

UGoDIT: Unsupervised Group Deep Image Prior Via Transferable Weights

Shijun Liang¹*, Ismail R. Alkhouri^{1,2}, Siddhant Gautam¹,
 Qing Qu², Saiprasad Ravishankar¹
¹Michigan State University
²University of Michigan

Recent advances in data-centric deep generative models have led to significant progress in solving inverse imaging problems. However, these models (e.g., diffusion models (DMs)) typically require large amounts of fully sampled (clean) training data, which is often impractical in medical and scientific settings such as dynamic imaging. On the other hand, training-data-free approaches like the Deep Image Prior (DIP) do not require clean ground-truth images but suffer from noise overfitting and can be computationally expensive as the network parameters need to be optimized for each measurement set independently. Moreover, DIP-based methods often overlook the potential of learning a prior using a small number of sub-sampled measurements (or degraded images) available during training. In this paper, we propose UGoDIT, an Unsupervised **Group DIP** via Transferable weights, designed for the low-data regime where only a very small number, M , of sub-sampled measurement vectors are available during training. Our method learns a set of transferable weights by optimizing a shared encoder and M disentangled decoders. At test time, we reconstruct the unseen degraded image using a DIP network, where part of the parameters are fixed to the learned weights, while the remaining are optimized to enforce measurement consistency. We evaluate UGoDIT on both medical (multi-coil MRI) and natural (super resolution and non-linear deblurring) image recovery tasks under various settings. Compared to recent standalone DIP methods, UGoDIT provides accelerated convergence and notable improvement in reconstruction quality. Furthermore, our method achieves performance competitive with SOTA DM-based and supervised approaches, despite not requiring large amounts of clean training data.

1. Introduction

Solving inverse problems are important across a wide range of practical applications, such as those in robotics [1], forensics [2], remote sensing [3], and geophysics [4]. One class of such problems is Inverse Imaging Problems (IIPs), including super-resolution [5], image denoising [6], image deblurring [7], recovering missing portions of images [8] (in-painting), and magnetic resonance imaging (MRI) reconstruction [9].

In recent years, an abundance of deep learning (DL) methods have been developed to solve IIPs [10–14]. Based on the availability of training data points, DL-based IIP methods can be categorized into (i) data-less DL approaches, such as the ones based on the Deep Image Prior (DIP) [15] and Implicit Neural Representation (INR) [16], and (ii) data-centric DL approaches, such as the ones based on supervised networks [17, 18], or generative models such as those based on diffusion models (DMs) [13, 14].

Data-centric methods rely on pre-trained models that typically require large-scale training datasets. In the context of scientific IIPs or medical IIPs such as MRI, in addition to being large-scale, this translates to the need for fully sampled measurements—i.e., clean images that serve as ground truth. Unlike natural images, however, acquiring large datasets of scientific or medical data such as fully

*The first two authors contributed equally.

sampled MRI scans is particularly challenging [19–21]. The underlying data may be inherently undersampled or corrupted with unknown noise. Similar issues arise in other domains such as medical computed tomography (CT) [22]. To mitigate this, previous DM-based methods for MRI and CT often fine-tune DMs pre-trained on natural images using a limited number of fully sampled medical images [12–14]. This underscores the need for approaches that reduce reliance on large, clean (or fully sampled) datasets.

Training-data-free methods, such as DIP [15], which rely on untrained networks (e.g., U-Net [23]), avoid the need for training data altogether—fully sampled or otherwise. However, they often face two main challenges: (i) vulnerability to noise overfitting (though recent variants, such as auto-encoding sequential DIP (aSeqDIP) [24], have shown improved robustness), and (ii) high computational cost at inference time (as a full set of network parameters need to be optimized for each measurement independently), especially compared to the inference time of supervised methods. Although recent work, such as MetaDIP [25], has explored transferring learned DIP weights to speed up inference, it still requires supervised training with fully sampled data points, and does not achieve competitive results when compared to standalone DIP methods as was demonstrated in [26].

The scarcity of fully-sampled measurements (i.e., clean images as ground truth) in certain applications, and the inability of most DIP methods to transfer learned weights serve as our motivation to explore the following question: *Is it possible to train a fully unsupervised model using only a few degraded images, such that the learned weights can later be used to reconstruct unseen measurements during inference?* We term the regime when only very few training images are available as the “low-data regime”, and towards answering the above question, we make the following contributions:

- **Decoder-disentangled architecture for training:** Given a few measurement vectors (or degraded images), we propose the use of a shared encoder and multiple decoders for each measurement vector during training such that the inputs, shared encoder, and multiple decoders are optimized jointly using a measurement-consistent and auto-encoded objective function.
- **Transferable weights at testing:** Given an unseen measurement vector, we transfer the pre-trained weights of the shared encoder to a single-encoder, single-decoder DIP network. Reconstruction is then performed by fixing the encoder and optimizing the decoder parameters using an input-adaptive, measurement-consistent objective function. Therefore, we term our method as Unsupervised Group DIP with Transferable weights (UGoDIT).
- **Extensive Evaluation:** We conduct extensive evaluations using multi-coil MRI, super resolution, and non-linear deblurring. We show that we outperform most recent advanced DIP methods while performing comparably with DM-based and supervised data-intensive methods all while requiring only a very few degraded images. Furthermore, our ablation studies show the impact of each component such as the proposed disentangled decoders.

2. Preliminaries & related work

Inverse Imaging Problems (IIPs) are defined as recovering an image $\mathbf{x}^* \in \mathbb{R}^n$ from measurement vector (or degraded image) $\mathbf{y} \in \mathbb{R}^m$ (with $m \leq n$), governed by the forward operator \mathbf{A} . For multi-coil MRI, the forward operator is given as $\mathbf{A} = \mathbf{MFS}$, for which \mathbf{M} denotes coil-wise undersampling, \mathbf{F} is the coil-by-coil Fourier transform, and \mathbf{S} represents the sensitivity encoding with multiple coils². For natural image restoration tasks, the forward operator in super resolution (SR) is a down sampler. For non-linear deblurring (NDB), the non-linear forward operator is the neural network approximated kernel given in [7] and adopted in multiple works such as [14, 27]. Next, we provide a brief overview of prior DL-based image reconstruction methods based on the availability of training data.

High-data regime methods: Training data-intensive methods—that is, methods that rely on a large number of training data points—can be categorized into generative, supervised, and unsupervised

²In MRI, the entries of \mathbf{x}^* and \mathbf{y} , contain both real and imaginary numbers. However, to generalize the definition of the problem, we use real numbers.

approaches. Among generative methods, recently, numerous IIP solvers have employed pre-trained diffusion models (DMs) as priors (e.g., [13, 14]; see [28] for a recent survey). These methods typically modify the reverse sampling steps to enable sampling from a measurement-conditioned distribution. In supervised end-to-end (E2E) approaches, a variety of techniques have been explored, including unrolled networks such as the variational network (VarNet) in [17]. A common limitation of both generative and supervised methods is their reliance not only on large amounts of training data, but also on clean (i.e., fully sampled) ground truth images—an assumption that may not hold in many medical and scientific applications such as MRI reconstruction³. Moreover, DM-based generative methods are generally slower at inference compared to supervised counterparts. Unsupervised (or self-supervised) methods have also been explored [30–32]. While they do not require clean images, they still depend on a large amount of training data and often fall short of the performance achieved by supervised or generative models. In this paper, we introduce a method that requires neither large-scale training data nor clean images (or fully sampled measurements) measurements.

Training-data-free methods: The pioneering work of [15] introduced the Deep Image Prior (DIP), a fully training-data-free approach for solving IIPs, demonstrating that an untrained convolutional neural network (CNN) can effectively recover low-frequency image structures using the implicit bias of the network. However, DIP is prone to noise overfitting due to the network’s over-parameterization. As a result, numerous techniques have been proposed to mitigate this issue, including the use of regularization [24, 33], early stopping [34], and network re-parameterization [26, 35]. We refer the reader to the recent tutorial in [36] for a comprehensive overview of DIP and its variants. Most DIP methods require optimizing a full set of weights for each measurement vector independently. In this paper, we present a DIP-based method that learns a subset of transferable weights from only a few degraded images, addressing this gap.

Low-data regime methods: Low-data regime refers to the case where the number of training images is extremely small for training standard supervised, generative, and/or unsupervised methods. Here, we discuss two methods that operate in the low-data regime and are closely related to our work. The first is MetaDIP [25], where the authors leverage meta-learning to fine-tune a set of hyper-parameters and learn transferable weights for accelerated DIP reconstruction at test time. MetaDIP adopts a standard single-encoder, single-decoder U-Net architecture. There are three key differences between UGoDIT and MetaDIP: (i) MetaDIP requires clean images during training, while our method uses only degraded images (or sub-sampled measurement vectors); (ii) MetaDIP does not include architectural changes during training; (iii) their evaluation is limited to natural image restoration tasks, whereas our method also considers more complex, large-scale MRI reconstruction. The second method is STRAINER [37], which extends the Implicit Neural Representation (INR) framework [38, 39] to the low-data regime. Specifically, the authors propose using a fully connected network (or multi-layer perceptron, MLP) with multiple output sub-networks to learn transferable weights. At test time, a subset of these weights is used to initialize a subset of the MLP-based INR model for image recovery. The main differences between UGoDIT and STRAINER are: (i) STRAINER uses MLPs with spatial coordinate input embedding, while our method is based on CNNs and DIP; (ii) STRAINER uses clean (fully sampled) training data, whereas UGoDIT uses degraded images (or sub-sampled measurements); (iii) the learned weights in STRAINER are used only for *initializing* part of the test-time INR network, whereas in our method, we keep the parameters of the pre-trained shared encoder unchanged during testing and only adapt the parameters of the test-time decoder.

3. Proposed method

Assume that we are given a set Y , consisting of M under-sampled measurement vectors (or degraded images), where each $\mathbf{y}_i \in Y$, for $i \in [M] := \{1, \dots, M\}$, is an m -dimensional vector. The degraded images in set Y are obtained using the following forward models: $\mathbf{y}_i = \mathbf{A}_i \mathbf{x}_i^* + \boldsymbol{\eta}_i$, where $\boldsymbol{\eta}_i$ represents the noise in the measurement domain, e.g., assumed sampled from a Gaussian distribution $\mathcal{N}(\mathbf{0}, \sigma_{\mathbf{y}_i}^2 \mathbf{I})$,

³We note that there have been recent efforts to train DMs on degraded images, such as the study in [29]. However, these approaches still rely on large amounts of training data.

where $\sigma_{\mathbf{y}_i} > 0$ denotes the noise level of the i -th vector. In this setting, we assume access only to \mathbf{y}_i and the corresponding \mathbf{A}_i for each $i \in [M]$. We note that while we adopt a linear forward model for notational simplicity, our approach can be applied to nonlinear IIPs, as we will demonstrate in our experimental results.

Here, the number of available training images, M , is extremely small (e.g., $M < 10$), making it infeasible to learn a data distribution to be used as a prior during inference. Under this under-sampled (or degraded), low-data regime, we consider the following question:

Given a CNN architecture and a set of M measurement vectors, $\mathbf{y}_i \in Y$, with corresponding forward operators \mathbf{A}_i , can we learn a set of weights such that, for a unseen test-time measurement vector $\mathbf{y} \notin Y$ and its operator \mathbf{A} , we can reconstruct the image both *robustly* and *efficiently*?

Here, *robust* reconstruction refers to achieving high-quality recovery while being resilient to noise overfitting—an issue commonly encountered in standalone DIP methods [33, 36]⁴. *Efficient* reconstruction refers to faster convergence compared to standalone DIP.

Among existing DIP methods, autoencoding Sequential DIP (aSeqDIP) [24] has demonstrated superior performance in terms of robustness and reconstruction quality. Meanwhile, Early Stopping DIP (ES-DIP) [34] and Deep Random Projector (DRP) [26] have shown improved efficiency in terms of faster run-time.

To enable the learning of transferable weights—which is the central goal of this paper—we propose the use of a modified network architecture: a shared encoder jointly learned across all M degraded images, along with a separate decoder for each individual measurement vector \mathbf{y}_i , resulting in M disentangled decoders. To mitigate noise overfitting, we adopt an input-adaptive autoencoding objective, which we describe in the next subsection. At test time, given an unseen vector \mathbf{y} , we use a DIP network, consisting of the learned shared encoder and a randomly initialized decoder, and perform image reconstruction by optimizing only the decoder parameters. In other words, given \mathbf{y} at test time, the pre-trained encoder is used to extract latent features and the decoder parameters are optimized to adapt to the unseen measurement vector.

We note that using a single encoder with multiple decoders has also been explored in other areas of machine learning, including multi-task and federated learning [40, 41]. Another example is [42], which proposed a multi-decoder architecture to accelerate the training of diffusion models.

3.1. Proposed training optimization and network architecture

Assume we are given a CNN network (e.g., a U-Net [23]). Let $h : \mathbb{R}^n \rightarrow \mathbb{R}^l$, parameterized by ϕ , denote the encoder function of the CNN—i.e., the **downsampler**, consisting of a stack of convolution and pooling layers that extracts and compresses features, with $l \ll n$. Similarly, let $g : \mathbb{R}^l \rightarrow \mathbb{R}^n$, parameterized by ψ , be the decoder function—i.e., the **upsampler**, comprising a stack of transposed convolution and/or interpolation layers that reconstruct the high-resolution output from the compressed representation.

Given some input $\mathbf{z} \in \mathbb{R}^n$, the network output is expressed as $g_\psi \circ h_\phi(\mathbf{z})$. Using this setting with some measurement vector \mathbf{y} and its forward operator \mathbf{A} , reconstruction via vanilla DIP [15] is formulated as in (1), where $\hat{\mathbf{x}}$ denotes the reconstructed image.

$$\hat{\phi}, \hat{\psi} = \underset{\phi, \psi}{\operatorname{argmin}} \| \mathbf{A} g_\psi \circ h_\phi(\mathbf{z}) - \mathbf{y} \|_2^2, \quad \hat{\mathbf{x}} = g_{\hat{\psi}} \circ h_{\hat{\phi}}(\mathbf{z}), \quad (1)$$

Given a set of M degraded measurements of images, $\mathbf{y}_i \in Y$, each associated with a forward operator \mathbf{A}_i for $i \in [M]$, the proposed UGoDIT method utilizes a shared encoder h_ϕ and a distinct decoder g_{ψ_i} for each training image. This results in a total of M disentangled decoders tailored to the individual measurement vector.

⁴Standalone DIP refers to the standard setting where a single measurement vector is used, and the network is optimized from randomly initialized parameters.

Algorithm 1 Training: Unsupervised Group DIP Transferable via weights (UGoDIT)

Input: Number of training images M , measurement vectors \mathbf{y}_i and forward operators \mathbf{A}_i for $i \in [M]$, number of input updates K , number of gradient updates N , regularization parameter λ , and learning rate β .

Output: Trained encoder weights $\hat{\phi}$.

Initialization: $\mathbf{z}_i \leftarrow \mathbf{A}_i^H \mathbf{y}_i$; $\phi, \psi_i \sim \mathcal{N}(\mathbf{0}, \sigma_{\text{ini}} \mathbf{I})$ for $i \in [M]$.

1: **For** K iterations, **Do**

2: **For** N iterations, **Do** (Shared encoder and M decoders parameters update)

3: $\psi_i \leftarrow \psi_i - \beta \nabla_{\psi_i} \left[\|\mathbf{A}_i g_{\psi_i} \circ h_{\phi}(\mathbf{z}_i) - \mathbf{y}_i\|_2^2 + \lambda \|g_{\psi_i} \circ h_{\phi}(\mathbf{z}_i) - \mathbf{z}_i\|_2^2 \right], \forall i \in [M]$

4: $\phi \leftarrow \phi - \beta \nabla_{\phi} \left[\sum_{i \in [M]} \|\mathbf{A}_i g_{\psi_i} \circ h_{\phi}(\mathbf{z}_i) - \mathbf{y}_i\|_2^2 + \lambda \|g_{\psi_i} \circ h_{\phi}(\mathbf{z}_i) - \mathbf{z}_i\|_2^2 \right]$.

5: **Obtain** $\mathbf{z}_i \leftarrow g_{\psi_i} \circ h_{\phi}(\mathbf{z}_i)$. (Network input update for each training image $i \in [M]$)

6: **Trained weights:** $\hat{\phi} \leftarrow \phi$

Given that we have M measurement vectors, choosing the input is not straightforward across a training set. Hence, we develop an input-adaptive approach. To this end, during training, we propose optimizing the weights of the shared-encoder, decoder-disentangled CNN architecture using the following objective:

$$\hat{\phi}, \hat{\psi}_i, \hat{\mathbf{z}}_i = \underset{\phi, \psi_i, \mathbf{z}_i, i \in [M]}{\operatorname{argmin}} \left\{ \sum_{i \in [M]} \|\mathbf{A}_i g_{\psi_i} \circ h_{\phi}(\mathbf{z}_i) - \mathbf{y}_i\|_2^2 \text{ s.t. } g_{\psi_i} \circ h_{\phi}(\mathbf{z}_i) = \mathbf{z}_i, \forall i \in [M] \right\}. \quad (2)$$

To solve (2), we initialize $\phi, \psi_i \sim \mathcal{N}(\mathbf{0}, \sigma_{\text{ini}}^2 \mathbf{I})$ and set $\mathbf{z}_i \leftarrow \mathbf{A}_i^H \mathbf{y}_i$ for all $i \in [M]$, where σ_{ini} corresponds to the standard deviation for initialization. We then perform the following alternating updates for K iterations (which corresponds to the number of network inputs updates):

$$\phi, \psi_1, \dots, \psi_M \leftarrow \underset{\phi, \psi_i, i \in [M]}{\operatorname{argmin}} \left[\sum_{i \in [M]} \|\mathbf{A}_i g_{\psi_i} \circ h_{\phi}(\mathbf{z}_i) - \mathbf{y}_i\|_2^2 + \lambda \|g_{\psi_i} \circ h_{\phi}(\mathbf{z}_i) - \mathbf{z}_i\|_2^2 \right], \quad (3a)$$

$$\mathbf{z}_i \leftarrow g_{\psi_i} \circ h_{\phi}(\mathbf{z}_i), \forall i \in [M], \quad (3b)$$

where λ is a regularization parameter. Similar to aSeqDIP [24], we alternate between two phases: (i) perform $N \ll K$ gradient updates to optimize the network parameters ϕ and ψ_i using the optimization in (3), and (ii) update the network inputs \mathbf{z}_i via forward passes. Specifically, each input \mathbf{z}_i is updated by passing it through the shared encoder h_{ϕ} and the corresponding decoder g_{ψ_i} .

In the training optimization of (3), the first term enforces the output of decoder i to be consistent with the measurements vector \mathbf{y}_i governed by \mathbf{A}_i . The second term is an autoencoding term that implicitly enforces the equality constraints in (2). It is used to mitigate noise overfitting by enforcing that the output of each decoder is approximately consistent with the updated input of that particular image \mathbf{z}_i as the optimization progresses.

In what follows, we provide a justification of how we relaxed (2) into the alternating optimization updates in (3). The general intuition stems from prior studies that highlight the impact of network inputs in DIP-based reconstruction [24, 33, 43], where the study in [24] shows that reconstruction quality improves when the network input is closer to the ground truth.

Assume that the iterates in (3) converge to $\phi^*, \psi_i^*, \mathbf{z}_i^*, \forall i \in [M]$. Then, according to the second equation in (3), for continuous mappings $g_{\psi_i} \circ h_{\phi}(\cdot), \forall i \in [M]$, we have $\mathbf{z}_i^* = g_{\psi_i^*} \circ h_{\phi^*}(\mathbf{z}_i^*)$. Substituting this into the first equation of (3), in the limit, we get $\phi^*, \psi_i^* = \underset{\phi, \psi_i, i \in [M]}{\operatorname{argmin}} \left\{ \sum_{i \in [M]} \|\mathbf{A}_i g_{\psi_i} \circ h_{\phi}(\mathbf{z}_i^*) - \mathbf{y}_i\|_2^2 \text{ s.t. } g_{\psi_i} \circ h_{\phi}(\mathbf{z}_i^*) = \mathbf{z}_i^*, \forall i \in [M] \right\}$, which corresponds to the minimizer of (2) given a fixed \mathbf{z}_i^* . For each decoder, the limit points of (3) correspond to the solution of a constrained version of vanilla DIP in (1). The constraint enforces additional prior that could alleviate overfitting. While it is not straightforward to use first-order gradient-based algorithms for solving (2) given the hard equality constraints, the limit points in the updates of (3) nevertheless minimize (2). Furthermore, the network input is updated by a sequential feed forward process without needing expensive gradient-based updates.

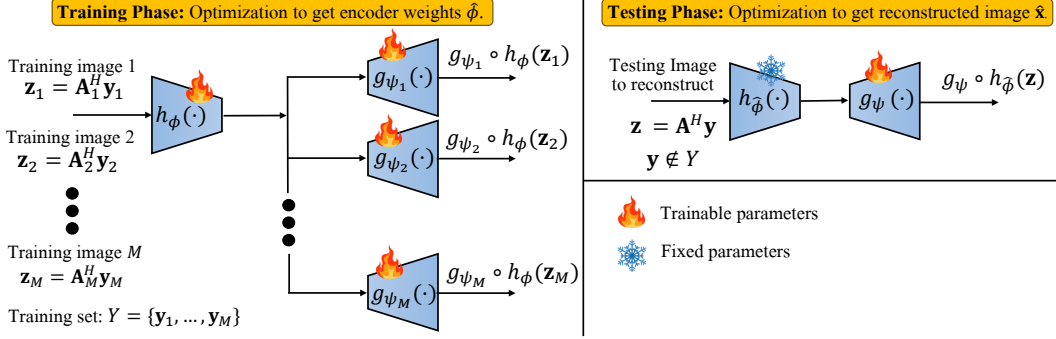


Figure 1: Illustrative block diagram UGoDIT. During training (*left*), we learn the shared encoder by optimizing over $\phi, \psi_1, \dots, \psi_M$. At inference (*right*), given some unseen measurement vector \mathbf{y} and its forward operator \mathbf{A} , we reconstruct the image $\hat{\mathbf{x}}$ by optimizing over ψ .

The training procedure of UGoDIT is given in Algorithm 1. In the initialization step, we assume the encoder and decoder weights are of equal size, though this is not necessary requirement. We emphasize that while steps 2 to 4 describe updating the network parameters using a fixed-step gradient descent, we use the ADAM optimizer [44], initialized with learning rate β . The computational requirements for training UGoDIT are determined by: (i) the NK gradient-based parameter updates, and (ii) the number of function evaluations (network forward passes) necessary for updating \mathbf{z}_i , which is MK . See Figure 1 (*left*) for an illustrative block diagram of the training phase.

Testing phase: Provided with the trained weights of the shared encoder, i.e., parameters $\hat{\phi}$ from Algorithm 1, and unseen measurement vector \mathbf{y} with its forward operator \mathbf{A} , at inference, we propose to use a new network mapping denoted by $h_{\hat{\phi}} \circ g_{\psi}(\cdot)$, where $\hat{\phi}$ is set to the trained weights $\hat{\phi}$. Then, ψ is initialized using the standard way. More specifically, we set $\mathbf{z} \leftarrow \mathbf{A}^H \mathbf{y}$, $\hat{\phi} \leftarrow \hat{\phi}$, and $\psi \sim \mathcal{N}(\mathbf{0}, \sigma_{\text{ini}}^2 \mathbf{I})$, and perform the following updates for K iterations.

$$\psi \leftarrow \underset{\psi}{\operatorname{argmin}} \left[\|\mathbf{A}g_{\psi} \circ h_{\hat{\phi}}(\mathbf{z}) - \mathbf{y}\|_2^2 + \lambda \|g_{\psi} \circ h_{\hat{\phi}}(\mathbf{z}) - \mathbf{z}\|_2^2 \right], \quad (4a)$$

$$\mathbf{z} \leftarrow g_{\psi} \circ h_{\hat{\phi}}(\mathbf{z}). \quad (4b)$$

In (4), we only optimize over ψ while the parameters of the pre-trained encoder are fixed (i.e., $\hat{\phi}$)⁵. Similar to the training algorithm, for every input update (i.e., second equation in (4)), we use $N \ll K$ gradient steps for the optimization in (4). The intuition of using the steps in (4) is the same as in aSeqDIP [24]. However, we emphasize that our goal here is different as in UGoDIT, the aim is to learn transferable weights for better and accelerated reconstructions at testing time. Algorithm 2 presents the procedure for solving (4). The training and testing phases of UGoDIT are illustrated in Figure 1.

3.2. Intuition behind using M decoders in the training of UGoDIT

In this subsection, we describe the rationale behind using M disentangled decoders in the UGoDIT training phase and how this design choice influences the quality of the learned encoder weights. Specifically, we aim to answer the following question: *Why does learning with multiple decoders result in a better shared encoder for test-time reconstruction?* To build this intuition, we first examine the standard architecture comprising a single encoder and a single decoder—denoted by $h_{\phi_s} \circ g_{\psi_s}(\cdot)$ —trained across M degraded images. The parameters are initialized as $\phi_s, \psi_s \sim \mathcal{N}(\mathbf{0}, \sigma_{\text{ini}}^2 \mathbf{I})$ and the inputs as $\mathbf{z}_i \leftarrow \mathbf{A}_i^H \mathbf{y}_i, \forall i \in [M]$. Then, we perform the following alternating optimization (which extends [24]

⁵In Appendix B, we conduct a study to show the difference between freezing the encoder (our method) and only initializing it (as was done in STRAINER [37]).

Algorithm 2 Testing: Unsupervised Group DIP Transferable via weights (UGoDIT- M)

Input: Pre-trained encoder weights $\hat{\phi}$ from Algorithm 1, measurement vector \mathbf{y} , forward operator \mathbf{A} , number of input updates K , number of gradient updates N , regularization parameter λ , and learning rate β .

Output: Reconstructed image $\hat{\mathbf{x}}$.

Initialization: $\mathbf{z} \leftarrow \mathbf{A}^H \mathbf{y}; \psi \sim \mathcal{N}(\mathbf{0}, \sigma_{\text{ini}} \mathbf{I})$.

1: **For** K iterations, **Do**

2: **For** N iterations, **Do** (Decoder parameters update)

3: $\psi \leftarrow \psi - \beta \nabla_{\psi} \left[\|\mathbf{A} g_{\psi} \circ h_{\hat{\phi}}(\mathbf{z}) - \mathbf{y}\|_2^2 + \lambda \|g_{\psi} \circ h_{\hat{\phi}}(\mathbf{z}) - \mathbf{z}\|_2^2 \right]$

4: **Obtain** $\mathbf{z} \leftarrow g_{\psi} \circ h_{\hat{\phi}}(\mathbf{z})$. (Network input update)

5: **Reconstructed Image:** $\hat{\mathbf{x}} \leftarrow g_{\psi} \circ h_{\hat{\phi}}(\mathbf{z})$

to $M > 1$ measurements vectors).

$$\phi_s, \psi_s \leftarrow \underset{\phi_s, \psi_s}{\operatorname{argmin}} \left[\sum_{i \in [M]} \|\mathbf{A}_i g_{\psi_s} \circ h_{\phi_s}(\mathbf{z}_i) - \mathbf{y}_i\|_2^2 + \lambda \|g_{\psi_s} \circ h_{\phi_s}(\mathbf{z}_i) - \mathbf{z}_i\|_2^2 \right], \quad (5a)$$

$$\mathbf{z}_i \leftarrow g_{\psi_s} \circ h_{\phi_s}(\mathbf{z}_i), \forall i \in [M]. \quad (5b)$$

Here, a single decoder g_{ψ_s} is shared across all training images. While the inputs \mathbf{z}_i are updated and initialized individually, they are all later optimized using the same encoder-decoder network. The gradient updates for this architecture are: $\psi_s \leftarrow \psi_s - \beta \nabla_{\psi_s} \left[\sum_{i \in [M]} \|\mathbf{A}_i g_{\psi_s} \circ h_{\phi_s}(\mathbf{z}_i) - \mathbf{y}_i\|_2^2 + \lambda \|g_{\psi_s} \circ h_{\phi_s}(\mathbf{z}_i) - \mathbf{z}_i\|_2^2 \right]$, and $\phi_s \leftarrow \phi_s - \beta \nabla_{\phi_s} \left[\sum_{i \in [M]} \|\mathbf{A}_i g_{\psi_s} \circ h_{\phi_s}(\mathbf{z}_i) - \mathbf{y}_i\|_2^2 + \lambda \|g_{\psi_s} \circ h_{\phi_s}(\mathbf{z}_i) - \mathbf{z}_i\|_2^2 \right]$.

From these expressions, the encoder h_{ϕ_s} is trained with using back-propagated updates from a single decoder. In contrast, in UGoDIT, the encoder receives supervision from M distinct decoders, each independently optimized to reconstruct a different training image (steps 3 and 4 in Algorithm 1). This over-parameterization allows each decoder to specialize in reconstructing its corresponding input, thereby improving the enforcement of measurement consistency across the training set.

Moreover, because the encoder must support multiple decoders reconstructing different training samples, it is encouraged to extract more generalizable and robust features. This leads to the intuition: *Encoders that yield more accurate reconstructions during training tend to reconstruct better during testing.* We empirically validate this claim in Section 4 by comparing both training and test-time reconstructions using a shared decoder versus disentangled decoders (our method).

4. Experimental results

We consider three tasks: MRI reconstruction from undersampled measurements, super resolution (SR), and non-linear deblurring (NDB). For MRI, we use the knee portion of the fastMRI dataset [20]. The forward model is $\mathbf{y} \approx \mathbf{A} \mathbf{x}^*$. The multi-coil data is obtained using 15 coils and is cropped to a resolution of 320×320 pixels. To simulate undersampling of the MRI k-space, we use a Cartesian sampling pattern with 4x and 8x acceleration factors (AF). Sensitivity maps for the coils are obtained using the BART toolbox [45]. For the tasks of SR and NDB, we use the FFHQ dataset [46]. For all three tasks, we test UGoDIT and baselines with 20 randomly selected degraded images. Backbone architectures are adopted from [23] and [47] for MRI and SR (and NDB), respectively. For evaluation metrics, we use the Peak Signal to Noise Ratio (PSNR), the Structural SIMilarity (SSIM) index [48], and run-time. For natural images, we also report LPIPS [49]. All the experiments are run on a single RTX5000 GPU machine. Further implementation details are provided in Appendix I. For training-data-free methods, we use three regularization-based recent methods, aSeqDIP [24], Self-Guided DIP [33], and Deep Random Projector [26] (as a DIP acceleration method), and one early stopping (ES) method, ES-DIP [34]. For data-driven MRI baselines, we use two recent SOTA DM-based methods, SITCOM-MRI [14] and DDS [12], and a very competitive supervised model, VarNet [17]. For natural images, we also use SITCOM [14], in addition to DPS [27] and STRAINER [37]. STRAINER is a representative of low-data regime methods. The selection criteria of these baselines

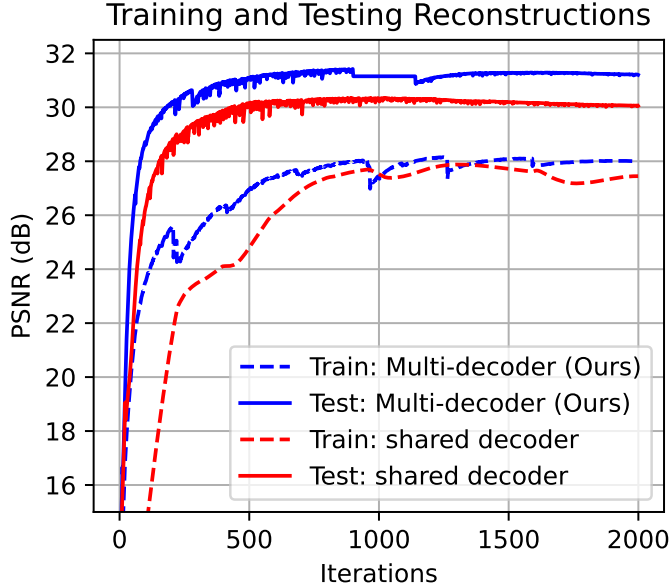


Figure 2: SR averaged PSNR curves of SR (6 for training and 20 for testing) of UGoDIT vs. the shared-decoder case (i.e., (5)).

depend on methods’ ability to achieve competitive reconstruction quality and high robustness to noise overfitting (for the case of DIP) for which several medical and natural image recovery tasks were considered (linear and non-linear). Baselines’ implementation details is given in Appendix I. For UGoDIT, we present results with three models, trained with 4, 5, and 6 degraded images (see Appendix F for results with $M > 6$). Our code is available online⁶. We test UGoDIT and other data-driven methods with in-distribution test instances, i.e., images from the testing sets of fastMRI and FFHQ. Out-of-distribution evaluation is provided in Appendix A. Ablation studies on the number of layers and the number of training images are given in Appendix E and Appendix F, respectively. Step size is set to $\beta = 0.0001$. The regularization parameter is set to $\lambda = 2$, following the study in Appendix C (where we also show the robustness to noise overfitting). For (N, K) , we use $(2, 2000)$, $(10, 2000)$, and $(10, 2000)$ for MRI, SR, and NDB, respectively, following the study in Appendix G.

Impact of using M decoders in UGoDIT: Here, we examine the effect of the multi-decoder architecture proposed in the training of UGoDIT. Specifically, we assess how using $M > 1$ disentangled decoders influences the quality of the shared encoder’s learned weights during both training and testing for the super resolution task. To this end, we compare our method against a baseline where $M = 6$ degraded images are trained using a standard single-encoder, single-decoder architecture, as described in (5). At inference, both approaches follow the procedure in (4) using their respective trained encoders. Figure 2 shows the average PSNR curves during training (dashed) and testing (solid with 20 test images) of UGoDIT and the shared-decoder case. As seen, employing multiple decoders yields approximately over a 1 dB to 1.5 dB improvement in both training and testing. These findings empirically support the rationale discussed in Section 3.2. Furthermore, we observe a gap of approximately 3 to 4 dB between the training and testing curves. We hypothesize that this arises because, during training, the network parameters are jointly optimized to reconstruct $M = 6$ images, whereas the testing curve reflects the average performance over 20 separate inference-time optimizations. Appendix D provides an additional study on the learned features of UGoDIT.

Comparison with DIP-based methods: Here, we aim to answer the question: *Given a set of degraded test images, does using UGoDIT offer any advantages over running a DIP-based method independently on each image?* Figure 3 presents the average PSNR curves, comparing UGoDIT (trained with 4, 5, and

⁶<https://github.com/sjames40/UGoDIT>

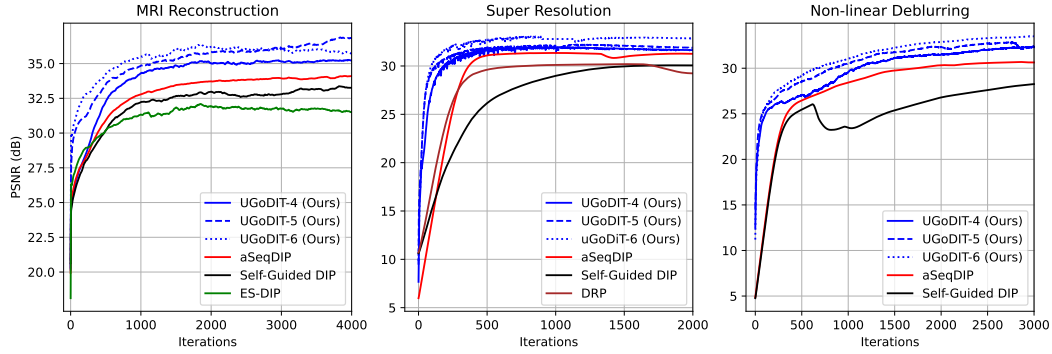


Figure 3: PSNR curves of UGoDIT- M and baselines for the tasks of MRI (left), SR (middle), and NDB (right) averaged over 20 test images. Iterations (x-axis) correspond to NK .

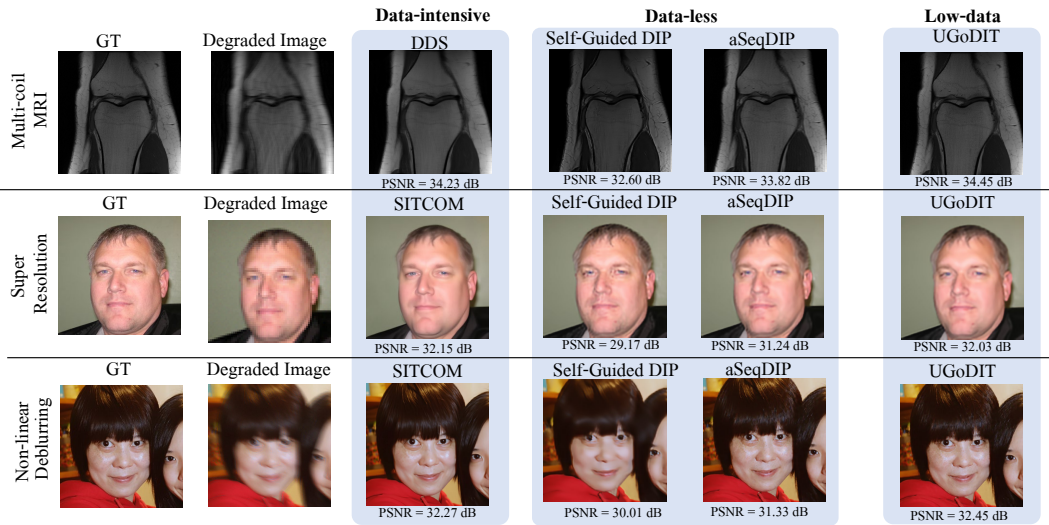


Figure 4: Reconstructed/recovered images using UGoDIT (last column) and baselines (columns 3 to 5). As observed, UGoDIT return comparable PSNR results with data-intensive methods all without the need of large amount of clean images (or fully sampled measurement vectors). See Appendix J for more visualizations.

6 degraded images) with four recent SOTA DIP baseline methods. In terms of PSNR improvements, UGoDIT achieves at least a 2 dB gain over aSeqDIP for MRI. For SR, we observe a marginal improvement—around 1 dB or slightly less—compared to aSeqDIP, but more than 2 dB over DRP and Self-Guided DIP. For NDB, UGoDIT consistently outperforms the second-best method (aSeqDIP) by at least 1 dB. Regarding acceleration, UGoDIT demonstrates a clear advantage in all three tasks, as measured by the number of iterations required to reach target PSNR values. For instance, in MRI, UGoDIT reaches 32.5 dB in 500 iterations or fewer, whereas aSeqDIP requires over 750 iterations to achieve the same PSNR. This trend also holds for SR and NDB. For example, in SR, UGoDIT-6 requires only about 125 steps to reach 30 dB, while aSeqDIP needs more than 250, and DRP nearly 600. Another noteworthy observation is that increasing the number of training images used by UGoDIT generally leads to better reconstruction quality. Collectively, these results highlight that UGoDIT provides improvements in both reconstruction performance and convergence speed.

Comparison with data-driven methods: Here, we compare UGoDIT with data-driven methods. Table 1 (resp. Table 2) presents the results for MRI (resp. SR and NDB). For MRI, all three variants of UGoDIT outperform DDS and VarNet in terms of PSNR, although they are slower. Compared to SITCOM-MRI, UGoDIT achieves slightly lower PSNR but is faster in terms of run-time. For SR and

| Method | Training images M | Type | Acceleration Factor (AF): 4x | | | Acceleration Factor (AF): 8x | | |
|-----------------|---------------------|---------------|------------------------------|---------------------|---------------------------|------------------------------|---------------------|---------------------------|
| | | | PSNR (\uparrow) | SSIM (\uparrow) | run-time (\downarrow) | PSNR (\uparrow) | SSIM (\uparrow) | run-time (\downarrow) |
| VarNet [17] | 8000 | Fully sampled | 33.06 \pm 0.59 | 0.854 \pm 0.12 | 5.02 \pm 2.12 | 32.03 \pm 0.35 | 0.829 \pm 0.08 | 5.45 \pm 2.11 |
| DDS [12] | 19460 | Fully sampled | 34.95 \pm 0.74 | 0.954 \pm 0.10 | 25.20 \pm 5.22 | 31.72 \pm 1.88 | 0.876 \pm 0.06 | 31.02 \pm 2.01 |
| SITCOM-MRI [14] | 19460 | Fully sampled | 36.33 \pm 0.37 | 0.962 \pm 0.08 | 76.24 \pm 6.25 | 32.78 \pm 0.64 | 0.892 \pm 0.02 | 82.45 \pm 4.20 |
| UGoDIT (Ours) | 4 | Sub-sampled | 35.45 \pm 0.34 | 0.957 \pm 0.08 | 45.20 \pm 4.20 | 32.04 \pm 0.45 | 0.878 \pm 0.06 | 47.42 \pm 5.64 |
| UGoDIT (Ours) | 5 | Sub-sampled | 35.74 \pm 0.41 | 0.959 \pm 0.09 | 48.12 \pm 5.42 | 32.36 \pm 0.51 | 0.881 \pm 0.06 | 48.12 \pm 3.24 |
| UGoDIT (Ours) | 6 | Sub-sampled | 36.05 \pm 0.34 | 0.960 \pm 0.08 | 48.42 \pm 5.40 | 32.54 \pm 0.45 | 0.883 \pm 0.06 | 49.33 \pm 7.44 |

Table 1: MRI reconstruction average results (with run-time in seconds) across two AFs of UGoDIT vs. data-centric methods. In SITCOM-MRI and DDS, the DM is trained on 973 MRI volumes each with 20 images. Column 3 corresponds to the “Type” of the training images. Values past \pm represent the standard deviation.

| Method | Training images M | Type | Super Resolution (SR) | | | | Non-linear Deblurring (NDB) | | | |
|---------------|---------------------|----------|-----------------------|---------------------|------------------------|---------------------------|-----------------------------|---------------------|------------------------|---------------------------|
| | | | PSNR (\uparrow) | SSIM (\uparrow) | LPIPS (\downarrow) | run-time (\downarrow) | PSNR (\uparrow) | SSIM (\uparrow) | LPIPS (\downarrow) | run-time (\downarrow) |
| DPS [27] | 49000 | Clean | 24.44 \pm 0.56 | 0.801 \pm 0.032 | 0.26 \pm 0.022 | 75.60 \pm 15.20 | 23.42 \pm 2.15 | 0.757 \pm 0.042 | 0.279 \pm 0.067 | 93.00 \pm 26.40 |
| SITCOM [14] | 49000 | Clean | 30.68 \pm 1.02 | 0.867 \pm 0.045 | 0.142 \pm 0.056 | 27.00 \pm 4.80 | 30.12 \pm 0.68 | 0.903 \pm 0.042 | 0.145 \pm 0.037 | 33.45 \pm 9.40 |
| STRAINER [37] | 4 | Clean | 29.03 \pm 1.30 | 0.841 \pm 0.12 | 0.189 \pm 0.045 | 32.12 \pm 6.20 | 27.20 \pm 1.30 | 0.812 \pm 0.21 | 0.201 \pm 0.055 | 33.40 \pm 7.24 |
| STRAINER [37] | 5 | Clean | 29.24 \pm 0.89 | 0.846 \pm 0.15 | 0.181 \pm 0.056 | 33.45 \pm 5.78 | 27.39 \pm 0.86 | 0.817 \pm 0.24 | 0.197 \pm 0.035 | 32.60 \pm 7.24 |
| STRAINER [37] | 6 | Clean | 29.45 \pm 0.56 | 0.849 \pm 0.08 | 0.177 \pm 0.041 | 31.12 \pm 6.20 | 27.41 \pm 0.56 | 0.819 \pm 0.043 | 0.189 \pm 0.048 | 30.50 \pm 4.67 |
| UGoDIT (Ours) | 4 | Degraded | 30.55 \pm 0.67 | 0.859 \pm 0.045 | 0.154 \pm 0.067 | 29.25 \pm 5.54 | 29.89 \pm 0.52 | 0.897 \pm 0.078 | 0.167 \pm 0.045 | 28.88 \pm 4.67 |
| UGoDIT (Ours) | 5 | Degraded | 30.62 \pm 0.38 | 0.863 \pm 0.067 | 0.149 \pm 0.035 | 30.15 \pm 6.74 | 30.09 \pm 0.37 | 0.899 \pm 0.057 | 0.156 \pm 0.035 | 29.29 \pm 3.78 |
| UGoDIT (Ours) | 6 | Degraded | 30.75 \pm 0.58 | 0.871 \pm 0.054 | 0.157 \pm 0.058 | 30.41 \pm 5.54 | 30.19 \pm 0.46 | 0.906 \pm 0.067 | 0.147 \pm 0.035 | 30.18 \pm 3.89 |

Table 2: Restoration results of UGoDIT vs. data-centric methods. Column 3 corresponds to the “Type” of the training images. Following [14, 27], we use $\sigma_{y_i} = 0.05, \forall, i \in [M]$ and $M \in \{4, 5, 6\}$. UGoDIT uses the degraded versions of the clean training images used for STRAINER. Values past \pm represent standard deviation.

NDB, UGoDIT achieves comparable PSNR performance to SITCOM. Compared to STRAINER, UGoDIT provides improvements of over 1 dB for SR and 2 dB for NDB, given similar run-times—importantly, without requiring clean images for training. Overall, these results demonstrate that UGoDIT can achieve competitive performance with SOTA data-driven methods, all without relying on large quantities of fully sampled (i.e., clean) training images. See also the visualizations Figure 4.

5. Conclusion

This paper introduced UGoDIT, a fully unsupervised framework for solving inverse imaging problems in the low-data regime, where only a very small number of degraded images are available during training. By learning a shared encoder with transferable weights across multiple decoders, UGoDIT effectively bridges the gap between the recent SOTA data-intensive generative models and training-data-free deep image prior (DIP) methods. Unlike DIP approaches that optimize a separate network per image, UGoDIT leverages the shared encoder to accelerate convergence and improve reconstruction quality. Empirical evaluations across MRI, super-resolution, and non-linear deblurring tasks show that UGoDIT achieves results comparable to SOTA supervised and diffusion-based methods, all without requiring access to a large number of clean ground-truth images. These results highlight the potential of UGoDIT as a data-efficient solution for inverse problems. Limitations and future works are discussed in Appendix H.

References

- [1] Dinesh Manocha and John F Canny. Efficient inverse kinematics for general 6r manipulators. *IEEE transactions on robotics and automation*, 10(5):648–657, 2002.
- [2] Shaofei Ren, Guorong Chen, Tiange Li, Qijun Chen, and Shaofan Li. A deep learning-based computational algorithm for identifying damage load condition: an artificial intelligence inverse problem solution for failure analysis. *Computer Modeling in Engineering & Sciences*, 117(3):287–307, 2018.
- [3] Aviad Levis, Pratul P Srinivasan, Andrew A Chael, Ren Ng, and Katherine L Bouman. Gravitationally lensed black hole emission tomography. In *Proceedings of the IEEE/CVF Conference on Computer Vision and Pattern Recognition*, pages 19841–19850, 2022.

- [4] Noori BniLam and Rafid Al-Khoury. Parameter identification algorithm for ground source heat pump systems. *Applied energy*, 264:114712, 2020.
- [5] Christian Ledig, Lucas Theis, Ferenc Huszár, Jose Caballero, Andrew Cunningham, Alejandro Acosta, Andrew Aitken, Alykhan Tejani, Johannes Totz, Zehan Wang, et al. Photo-realistic single image super-resolution using a generative adversarial network. In *Proceedings of the IEEE conference on computer vision and pattern recognition*, pages 4681–4690, 2017.
- [6] B. Goyal, A. Dogra, S. Agrawal, B.S. Sohi, and A. Sharma. Image denoising review: From classical to state-of-the-art approaches. *Information Fusion*, 55:220–244, 2020. ISSN 1566-2535. doi: <https://doi.org/10.1016/j.inffus.2019.09.003>. URL <https://www.sciencedirect.com/science/article/pii/S1566253519301861>.
- [7] Phong Tran, Anh Tuan Tran, Quynh Phung, and Minh Hoai. Explore image deblurring via encoded blur kernel space. In *Proceedings of the IEEE/CVF conference on computer vision and pattern recognition*, pages 11956–11965, 2021.
- [8] O. Elharrouss, N. Almaadeed, S. Al-Maadeed, and Y. Akbari. Image inpainting: A review. *Neural Processing Letters*, 51:2007–2028, 2020.
- [9] J. A. Fessler. Model-Based Image Reconstruction for MRI. *IEEE Signal Processing Magazine*, 27(4):81–89, 2010. doi: 10.1109/MSP.2010.936726.
- [10] Michael T McCann, Kyong Hwan Jin, and Michael Unser. Convolutional neural networks for inverse problems in imaging: A review. *IEEE Signal Processing Magazine*, 34(6):85–95, 2017.
- [11] Ismail Alkhouri, Shijun Liang, Rongrong Wang, Qing Qu, and Saiprasad Ravishankar. Diffusion-based adversarial purification for robust deep mri reconstruction. In *IEEE International Conference on Acoustics, Speech and Signal Processing (ICASSP)*, pages 12841–12845. IEEE, 2024.
- [12] Hyungjin Chung, Suhyeon Lee, and Jong Chul Ye. Decomposed diffusion sampler for accelerating large-scale inverse problems. In *ICLR*, 2024.
- [13] Hyungjin Chung and Jong Chul Ye. Score-based diffusion models for accelerated mri. *Medical image analysis*, 80:102479, 2022.
- [14] Ismail Alkhouri, Shijun Liang, Cheng-Han Huang, Jimmy Dai, Qing Qu, Saiprasad Ravishankar, and Rongrong Wang. Sitcom: Step-wise triple-consistent diffusion sampling for inverse problems. *ICML*, 2025.
- [15] Dmitry Ulyanov, Andrea Vedaldi, and Victor Lempitsky. Deep image prior. In *Proceedings of the IEEE conference on computer vision and pattern recognition*, pages 9446–9454, 2018.
- [16] Vishwanath Saragadam, Daniel LeJeune, Jasper Tan, Guha Balakrishnan, Ashok Veeraraghavan, and Richard G Baraniuk. Wire: Wavelet implicit neural representations. In *Proceedings of the IEEE/CVF Conference on Computer Vision and Pattern Recognition*, pages 18507–18516, 2023.
- [17] Anuroop Sriram, Jure Zbontar, Tullie Murrell, Aaron Defazio, C Lawrence Zitnick, Nafissa Yakubova, Florian Knoll, and Patricia Johnson. End-to-end variational networks for accelerated mri reconstruction. In *Medical Image Computing and Computer Assisted Intervention–MICCAI 2020: 23rd International Conference, Lima, Peru, October 4–8, 2020, Proceedings, Part II 23*, pages 64–73. Springer, 2020.
- [18] H. K. Aggarwal, M. P. Mani, and M. Jacob. Modl: Model-based deep learning architecture for inverse problems. *IEEE transactions on medical imaging*, 38(2):394–405, 2018.
- [19] Elisabeth R Garwood, Michael P Recht, and Lawrence M White. Advanced imaging techniques in the knee: benefits and limitations of new rapid acquisition strategies for routine knee MRI. *American Journal of Roentgenology*, 209(3):552–560, 2017.

- [20] J. Zbontar, F. Knoll, A. Sriram, T. Murrell, Z. Huang, M. J. Muckley, A. Defazio, R. Stern, P. Johnson, M. Bruno, et al. fastMRI: An open dataset and benchmarks for accelerated MRI. *arXiv preprint arXiv:1811.08839*, 2018.
- [21] Akshay S Chaudhari, Feliks Kogan, Valentina Pedoia, Sharmila Majumdar, Garry E Gold, and Brian A Hargreaves. Rapid knee MRI acquisition and analysis techniques for imaging osteoarthritis. *Journal of Magnetic Resonance Imaging*, 52(5):1321–1339, 2020.
- [22] Muhammad Shafique, Sizhuo Liu, Philip Schniter, and Rizwan Ahmad. Mri recovery with self-calibrated denoisers without fully-sampled data. *Magnetic Resonance Materials in Physics, Biology and Medicine*, 38:53–66, 2025. doi: 10.1007/s10334-024-01207-1.
- [23] Olaf Ronneberger, Philipp Fischer, and Thomas Brox. U-net: Convolutional networks for biomedical image segmentation. In *Medical image computing and computer-assisted intervention–MICCAI 2015: 18th international conference, Munich, Germany, October 5-9, 2015, proceedings, part III 18*, pages 234–241. Springer, 2015.
- [24] Ismail R. Alkhouri, Shijun Liang, Evan Bell, Qing Qu, Rongrong Wang, and Saiprasad Ravishankar. Image reconstruction via autoencoding sequential deep image prior. In *Advances in Neural Information Processing Systems*, volume 37, pages 18988–19012, 2024.
- [25] Kevin Zhang, Mingyang Xie, Maharshi Gor, Yi-Ting Chen, Yvonne Zhou, and Christopher A. Metzler. Metadip: Accelerating deep image prior with meta learning, 2022. URL <https://arxiv.org/abs/2209.08452>.
- [26] Taihui Li, Hengkang Wang, Zhong Zhuang, and Ju Sun. Deep random projector: Accelerated deep image prior. In *Proceedings of the IEEE/CVF Conference on Computer Vision and Pattern Recognition*, pages 18176–18185, 2023.
- [27] Hyungjin Chung, Jeongsol Kim, Michael Thompson Mccann, Marc Louis Klasky, and Jong Chul Ye. Diffusion posterior sampling for general noisy inverse problems. In *The Eleventh International Conference on Learning Representations*, 2023.
- [28] Giannis Daras, Hyungjin Chung, Chieh-Hsin Lai, Yuki Mitsufuji, Peyman Milanfar, Alexandros G. Dimakis, Chul Ye, and Mauricio Delbracio. A survey on diffusion models for inverse problems. 2024. URL https://giannisdaras.github.io/publications/diffusion_survey.pdf.
- [29] Asad Aali, Giannis Daras, Brett Levac, Sidharth Kumar, Alexandros G Dimakis, and Jonathan I Tamir. Ambient diffusion posterior sampling: Solving inverse problems with diffusion models trained on corrupted data. *ICLR*, 2025.
- [30] Jaakko Lehtinen, Jacob Munkberg, Jon Hasselgren, Samuli Laine, Tero Karras, Miika Aittala, and Timo Aila. Noise2noise: Learning image restoration without clean data. In *International Conference on Machine Learning*, pages 2965–2974. PMLR, 2018.
- [31] Zhihao Xia and Ayan Chakrabarti. Training image estimators without image ground truth. In H. Wallach, H. Larochelle, A. Beygelzimer, F. d’Alché-Buc, E. Fox, and R. Garnett, editors, *Advances in Neural Information Processing Systems*, volume 32. Curran Associates, Inc., 2019. URL https://proceedings.neurips.cc/paper_files/paper/2019/file/0ed9422357395a0d4879191c66f4faa2-Paper.pdf.
- [32] Jiaming Liu, Yu Sun, Cihat Eldeniz, Weijie Gan, Hongyu An, and Ulugbek S. Kamilov. Rare: Image reconstruction using deep priors learned without groundtruth. *IEEE Journal of Selected Topics in Signal Processing*, 14(6):1088–1099, 2020. doi: 10.1109/JSTSP.2020.2998402.
- [33] Shijun Liang, Evan Bell, Qing Qu, Rongrong Wang, and Saiprasad Ravishankar. Analysis of deep image prior and exploiting self-guidance for image reconstruction. *IEEE Transactions on Computational Imaging*, 11:435–451, 2025. ISSN 2333-9403. doi: 10.1109/TCI.2025.3540706.

- [34] Hengkang Wang, Taihui Li, Zhong Zhuang, Tiancong Chen, Hengyue Liang, and Ju Sun. Early stopping for deep image prior. *Transactions on Machine Learning Research*, 2023.
- [35] R Heckel et al. Deep decoder: Concise image representations from untrained non-convolutional networks. In *International Conference on Learning Representations*, 2019.
- [36] Ismail Alkhouri, Evan Bell, Avrajit Ghosh, Shijun Liang, Rongrong Wang, and Saiprasad Ravishankar. Understanding untrained deep models for inverse problems: Algorithms and theory. *arXiv preprint arXiv:2502.18612*, 2025.
- [37] Kushal Kardam Vyas, Imtiaz Humayun, Aniket Dashpute, Richard Baraniuk, Ashok Veeraraghavan, and Guha Balakrishnan. Learning transferable features for implicit neural representations. *Advances in Neural Information Processing Systems*, 37:42268–42291, 2024.
- [38] Vincent Sitzmann, Julien Martel, Alexander Bergman, David Lindell, and Gordon Wetzstein. Implicit neural representations with periodic activation functions. *Advances in neural information processing systems*, 33:7462–7473, 2020.
- [39] Zhiqin Chen and Hao Zhang. Learning implicit fields for generative shape modeling. In *Proceedings of the IEEE/CVF conference on computer vision and pattern recognition*, pages 5939–5948, 2019.
- [40] Deblina Bhattacharjee, Tong Zhang, Sabine Süssstrunk, and Mathieu Salzmann. Mult: An end-to-end multitask learning transformer. In *Proceedings of the IEEE/CVF conference on computer vision and pattern recognition*, pages 12031–12041, 2022.
- [41] Jingxuan Zhou, Weidong Bao, Ji Wang, Dayu Zhang, Xiongtao Zhang, and Yaohong Zhang. Multi-task federated learning with encoder-decoder structure: Enabling collaborative learning across different tasks. *arXiv preprint arXiv:2504.09800*, 2025.
- [42] Huijie Zhang, Yifu Lu, Ismail Alkhouri, Saiprasad Ravishankar, Dogyoon Song, and Qing Qu. Improving training efficiency of diffusion models via multi-stage framework and tailored multi-decoder architecture. In *Proceedings of the IEEE/CVF Conference on Computer Vision and Pattern Recognition (CVPR)*, pages 7372–7381, June 2024.
- [43] Di Zhao, Feng Zhao, and Yongjin Gan. Reference-driven compressed sensing mr image reconstruction using deep convolutional neural networks without pre-training. *Sensors*, 20(1):308, 2020.
- [44] Diederik P. Kingma and Jimmy Ba. Adam: A method for stochastic optimization. *arXiv preprint arXiv:1412.6980*, 2014.
- [45] J. I. Tamir, F. Ong, J. Y. Cheng, M. Uecker, and M. Lustig. Generalized magnetic resonance image reconstruction using the berkeley advanced reconstruction toolbox. In *ISMRM Workshop on Data Sampling & Image Reconstruction, Sedona, AZ*, 2016.
- [46] Tero Karras, Samuli Laine, and Timo Aila. A style-based generator architecture for generative adversarial networks. In *Proceedings of the IEEE/CVF conference on computer vision and pattern recognition*, pages 4401–4410, 2019.
- [47] Alejandro Newell, Kaiyu Yang, and Jia Deng. Stacked hourglass networks for human pose estimation. In *Computer Vision—ECCV 2016: 14th European Conference, Amsterdam, The Netherlands, October 11–14, 2016, Proceedings, Part VIII 14*, pages 483–499. Springer, 2016.
- [48] Zhou Wang, Alan C Bovik, Hamid R Sheikh, and Eero P Simoncelli. Image quality assessment: from error visibility to structural similarity. *IEEE transactions on image processing*, 13(4):600–612, 2004.

- [49] Richard Zhang, Phillip Isola, Alexei A Efros, Eli Shechtman, and Oliver Wang. The unreasonable effectiveness of deep features as a perceptual metric. In *Proceedings of the IEEE conference on computer vision and pattern recognition*, pages 586–595, 2018.
- [50] Jia Deng, Wei Dong, Richard Socher, Li-Jia Li, Kai Li, and Li Fei-Fei. Imagenet: A large-scale hierarchical image database. In *2009 IEEE conference on computer vision and pattern recognition*, pages 248–255. Ieee, 2009.

Appendix

In the Appendix, we first present two experiments to evaluate the out-of-distribution performance of UGoDIT (Appendix A). Appendix B examines the impact of freezing the encoder weights at test time, followed by a study on robustness to noise overfitting (Appendix C). Appendix D investigates the learned features in an MRI-trained UGoDIT model. This is followed by ablation studies on the number of convolutional layers (Appendix E), the number of training images M (Appendix F), and the choice of N and K (Appendix G). Limitations and future directions are discussed in Appendix H. Appendix I provides implementation details of the baselines, followed by a set of figures for additional visualizations (Appendix J).

A. Out-of-distribution evaluation

A.1. MRI

In this section, we investigate the out-of-distribution (OOD) capabilities of UGoDIT for the task of MRI. Specifically, we evaluate the encoder of UGoDIT-6 (which we will refer to as UGoDIT-OOD) trained on knee scans with 20 brain MRI test scans randomly selected from the fastMRI brain dataset.

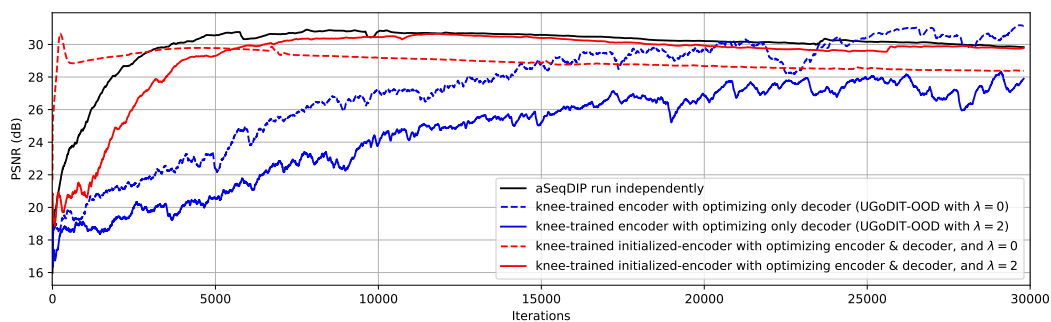


Figure 5: Average PSNR of 20 MRI brain test scans using a knee-trained (with $M = 6$) UGoDIT-OOD (blue) vs. the case where at test-time, we use the parameters of the pre-trained encoder to only initialize the test-time encoder (red). Then, we optimize over both the encoder and decoder. Running aSeqDIP independently is also included (black). Iterations in the x-axis correspond to $NK = 30000$.

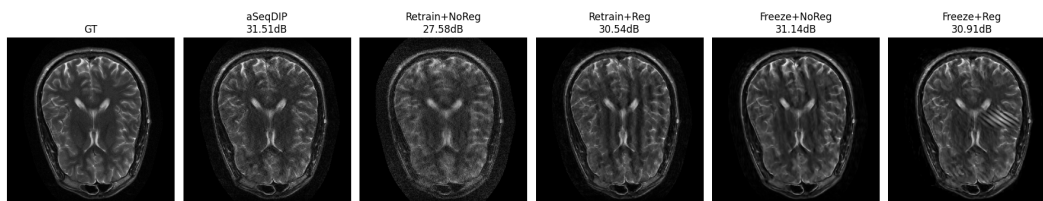


Figure 6: Brain reconstructed images for the OOD experiment. The titles of the third to fifth reconstructed images correspond to the dashed blue (UGoDIT-OOD with $\lambda = 0$), solid blue (UGoDIT-OOD with $\lambda = 2$), dashed red, and solid red curves, respectively, in the legend of Figure 5. PSNR values are given on the top of each reconstructed image.

The average PSNR curves are shown in Figure 5. As observed, when compared to aSeqDIP—which is run independently from scratch on each test scan (black curve)—the encoder trained on knee images under-performs and converges very slowly on brain scans.

We hypothesize that the autoencoding term and the input updates in UGoDIT—which implicitly enforce consistency between encoder-decoder input/output pairs—lead to the learning of features

that are overly tailored to the training distribution. As a result, when the test distribution differs significantly, these learned features make the convergence slower.

More specifically, when training and test images come from the same distribution (i.e., anatomy), the input updates and autoencoding term help reconstruction, as they promote alignment of shared low-frequency structures. However, under distribution shift (i.e., when the training and testing anatomies are different), these mechanisms degrade performance, since training and test images no longer share similar low-frequency content.

To support this hypothesis, Figure 5 includes two additional cases: (i) using the knee-trained encoder while optimizing only the decoder and setting $\lambda = 0$ (i.e., no autoencoding regularization in the first term of Eq. (4); shown as the dashed blue curve); and (ii) initializing the encoder with knee-trained weights and optimizing both the encoder and decoder, with $\lambda \in 0, 2$ (shown in red curves).

As observed, when $\lambda = 0$ (i.e., dashed curves), the results could be better than when $\lambda \neq 0$ as the input will have less impact. Furthermore, when we compare UGoDIT-ODD with only initializing the encoder (the red curves), the results are further improved which indicate that pre-trained weights on knees have less impact when only initialization is used. This is even more evident in the case when $\lambda = 0$ with initialization only (i.e., red dashed curve).

The visualizations in Figure 6 (which are recorded at iteration 30000) show that the all the considered cases would converge to between 27.58 dB to 31.51 dB.

A.2. Super Resolution

In this section, we investigate the OOD capabilities of UGoDIT on natural images for the task of super resolution (SR). To this end, we test the encoder of UGoDIT (trained with $M = 6$ images from the FFHQ dataset) with 20 degraded images randomly selected from the ImageNet dataset [50].

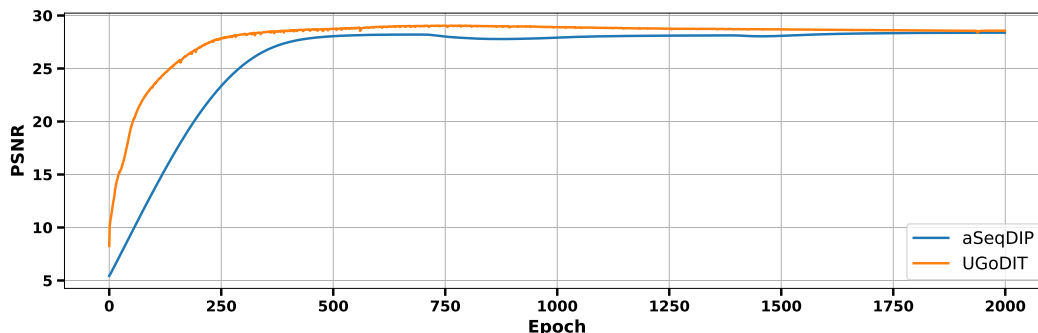


Figure 7: Average PSNR of 20 test images from the **ImageNet** dataset of UGoDIT trained with $M = 6$ **FFHQ** degraded images. Iterations in the x-axis correspond to $NK = 20000$.

For SR, We observe that UGoDIT-ODD slightly achieves better PSNR that eventually converges to similar PSNR values. However, unlike the MRI case, UGoDIT-ODD converges faster than aSeqDIP. This can also be observed in the restored images of Figure 8 and Figure 9. We attribute UGoDIT’s ability to generalize well to learning multi-frequency features under OOD scenario for the natural image.

B. Impact of freezing the test-time encoder in UGoDIT

Here, we show the impact of freezing the weights of the pre-trained encoder at test time. More specifically, given a pre-trained encoder with weight $\hat{\phi}$, we compare UGoDIT at test time with an alternative approach that initializes the test-time encoder with $\hat{\phi}$ and then optimizes both the encoder and decoder. We note that this is a similar setting to how the pre-trained MLP weights were used in STRAINER [37].

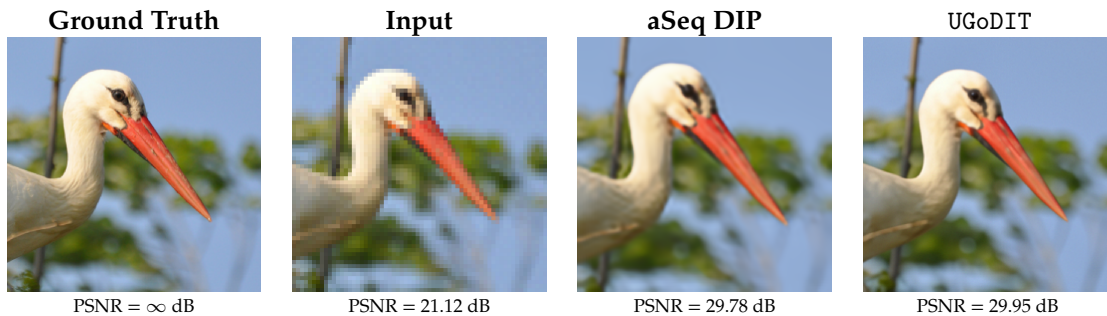


Figure 8: Ground-truth, degraded, and restored images for the OOD experiment on the task of super resolution, where UGoDIT was trained on 6 images of faces from the FFHQ dataset and tested on the ImageNet degraded image in the second column. As observed, the testing set is not a human face as is the case for the training images in FFHQ.

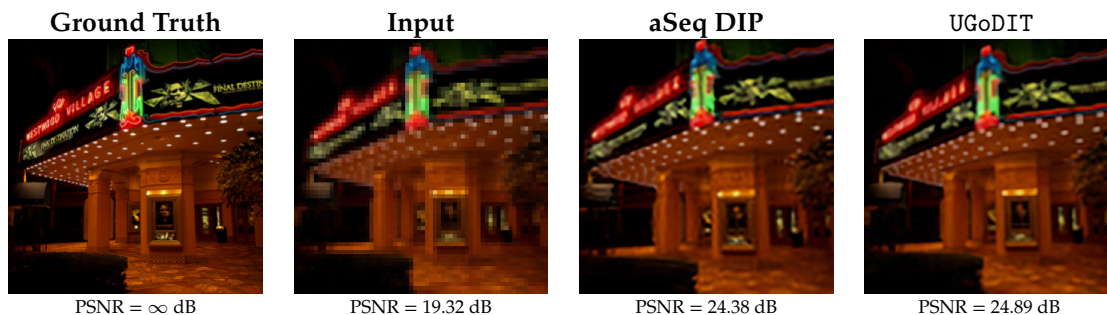


Figure 9: Ground-truth, degraded, and restored images for the OOD experiment on the task of super resolution, where UGoDIT was trained on 6 images of faces from the FFHQ dataset and tested on the ImageNet degraded image in the second column. As observed, the testing set is not a human face as is the case for the training images in FFHQ.

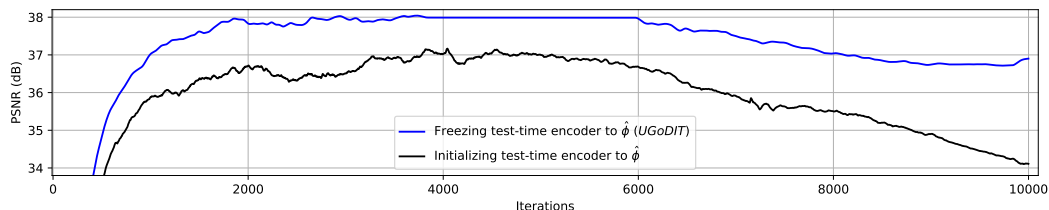


Figure 10: Average PSNR of 20 MRI test scans of UGoDIT-6 vs. the case where we use the parameters of the pre-trained encoder to only initialize the test-time encoder. Then, the optimization takes place over both the encoder and decoder. Iterations in the x-axis correspond to $NK = 10000$. For both cases, we use $\lambda = 2$.

Figure 10 presents the average PSNR over 20 MRI scans. As shown, freezing the encoder weights yields better results in terms of both PSNR (around 1dB difference) and convergence speed. Specifically, UGoDIT approaches the peak performance in approximately 2000 iterations. Moreover, UGoDIT requires optimizing fewer test-time parameters compared to the approach that initializes the encoder and optimizes both the encoder and decoder.

C. Robustness to noise overfitting and the impact of the regularization parameter λ

In this section, we demonstrate how UGoDIT is robust to noise overfitting, typically encountered in DIP-based methods. To this end, for the task of MRI reconstruction, we train UGoDIT with $M = 6$ knee scans across different values of the regularization parameter: $\lambda \in \{0.1, 1, 2, 10\}$. During testing, we use 20 scans.

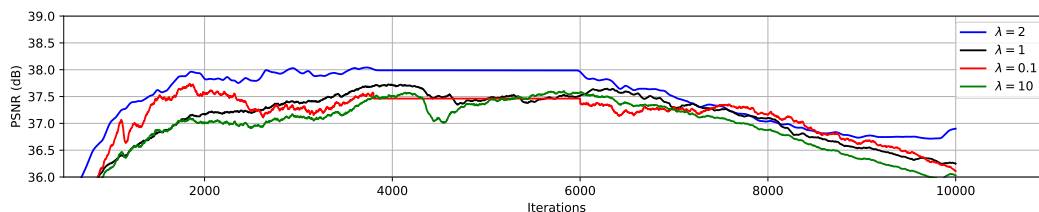


Figure 11: Average PSNR of 20 MRI test scans of UGoDIT-6 using different values of the regularization parameter λ at training and testing. Iterations in the x-axis correspond to $NK = 10000$.

Figure 11 presents the average PSNR during testing. As observed, even when we run our method for 10000 iterations, the PSNR drops by approximately less than 1.5 dB. This indicates that noise overfitting takes place but is minimal given the large number of iterations.

Additionally, the case of $\lambda = 2$ returns the highest PSNR and has the least noise overfitting (as indicated by the drop in PSNR). We also observe that the difference in PSNR across different λ 's is approximately 1 dB. This indicates that the performance of UGoDIT is not highly sensitive to the choice of the regularization parameter. In other words, if different values of λ are used (between 0.1 and 10), the PSNR value does not change significantly.

D. A study on the learned features in UGoDIT

To better understand the representations learned by our shared encoder, we examine the feature maps from its first few convolutional layers across two different approaches - one with the proposed UGoDIT framework and the other with the shared decoder (called single E-D) framework. To analyze the frequency content of the learned features, we applied a 2D Fourier transform to each channel of the encoder's layer and visualized the corresponding magnitude spectra. We computed a low-frequency (LF) magnitude ratio, which is the proportion of spectral energy contained within a central region of the frequency domain. This helps us to quantify, to how much extent, low frequency features dominate the learned representation. The LF magnitude ratio can be defined as

$$\text{LF ratio} = \frac{\sum_c \sum_{(u,v) \in \mathcal{C}} |\hat{x}_c[u, v]|}{\sum_c \sum_{(u,v)} |\hat{x}_c[u, v]|} \quad (6)$$

where $\hat{x}_c[u, v]$ is the 2D Fourier transform of the feature map at channel c , and \mathcal{C} is a centered square region in frequency space corresponding to low frequencies.

Table 3 summarizes the low-frequency (LF) magnitude ratios computed for 2 images across four encoder layers and the decoder output, along with PSNR (in dB). These results are reported for

| Metric | Slice 1 | | Slice 2 | |
|----------------|--------------|--------------|--------------|--------------|
| | UGoDIT | Single E-D | UGoDIT | Single E-D |
| First Layer | 0.463 | 0.525 | 0.363 | 0.417 |
| Second Layer | 0.341 | 0.318 | 0.302 | 0.325 |
| Third Layer | 0.235 | 0.337 | 0.233 | 0.357 |
| Fourth Layer | 0.166 | 0.232 | 0.207 | 0.303 |
| Decoder Output | 0.475 | 0.500 | 0.503 | 0.534 |
| PSNR (dB) | 36.61 | 33.98 | 35.92 | 34.82 |

Table 3: Comparison of low-frequency (LF) magnitude ratios and PSNR for UGoDIT and the Single E-D approach for MRI reconstruction at $4\times$ acceleration factor. The first five rows report LF magnitude ratios from encoder layers and the decoder output; the last row reports PSNR (in dB). For reference, the LF magnitude ratios for the ground truth images are 0.412 (Slice 1) and 0.439 (Slice 2).

both the UGoDIT and Single E-D (one encoder, one decoder) approaches that were used for MRI reconstruction at $4\times$ acceleration factor. Across both test slices, Single E-D exhibits higher LF magnitude ratios in most layers, including the decoder output, indicating a stronger low-frequency bias. UGoDIT achieves higher PSNR values for both slices that have only moderate low-frequency content. Its feature representations better capture high-frequency details in the image and yield better final reconstructed images than the single E-D case, which shows a more pronounced low-frequency bias from shared training.

E. Impact of the number of convolutional layers in the architecture of UGoDIT

In this section, we analyze the impact of varying the depth of the convolutional blocks in UGoDIT. Specifically, we evaluate five different configurations of the Skip-net architecture [47] on the super-resolution task performance, each with a different number of upsampling and downsampling convolutional layers, and report the resulting PSNR values.

As shown in Figure 12, the configuration with five convolutional layers in both the encoder and decoder produces the highest and most stable PSNR. Increasing the number of layers beyond five yields no further improvement, while reducing the layer count leads to a noticeable degradation in PSNR.

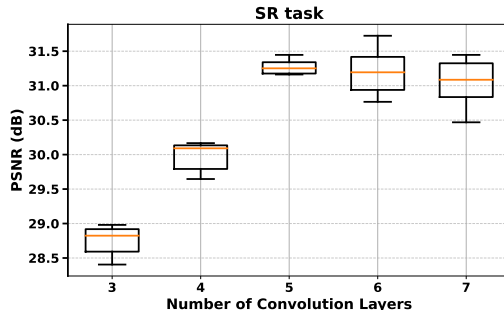


Figure 12: Ablation study in terms of PSNR as a function of the number of Convolution layers in the Skip Net for the Super Resolution task, averaged over 20 test images. The x-axis indicates the number of convolutional layers in each of the upsampling and downsampling parts of the network architecture.

F. Impact of the number of training images (M) in UGoDIT

In this section, we investigate how the size of the training set influences UGoDIT’s performance. To this end, we consider the non-linear deblurring task and train the shared encoder using five different FFHQ-derived subsets [46], and evaluate each on the same deblurring benchmark. As shown in Figure 13, performance steadily improves as we increase the number of training images, peaking at six images—beyond which additional data yields negligible gains.

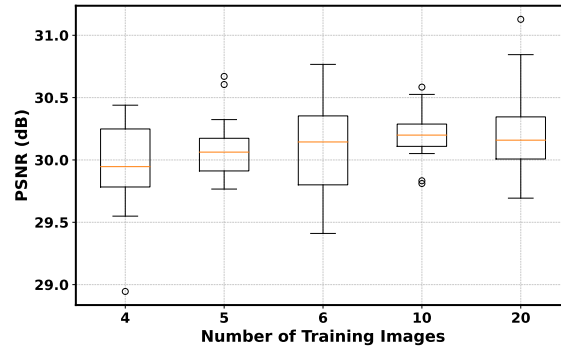


Figure 13: Ablation study on the number of training images, M , as given in Algorithm 1 and Algorithm 2. Results are averaged over 20 images for the task of NDB.

G. Ablation study on N and K in UGoDIT

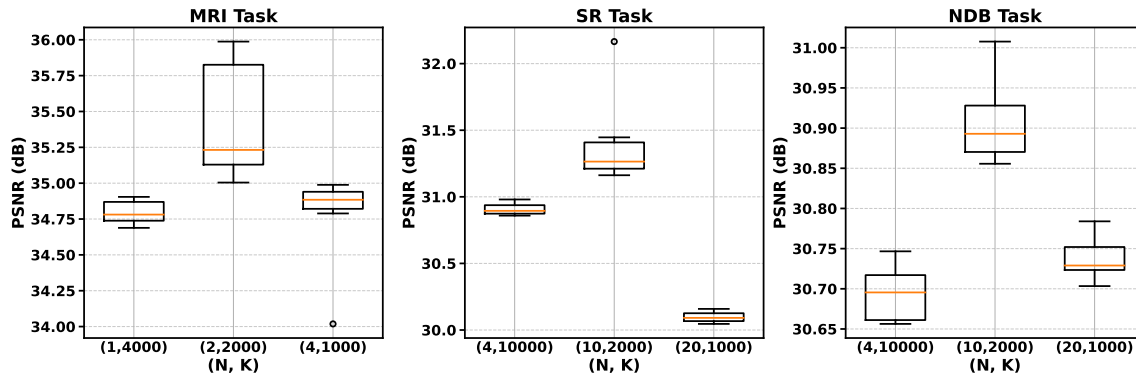


Figure 14: Ablation study on the number of gradient updates, N , for every inputs updates, K , as given in Algorithm 1 and Algorithm 2. Results are given as the average of 20 images for the tasks of MRI (left), SR (middle), and NDB (right).

Here, we conduct an ablation study on the number of gradient updates, N , for each inputs updates (i.e., K) in the training (Algorithm 1) and testing (Algorithm 2) of UGoDIT.

The results are given presented in Figure 14, where we report the average PSNR values across the tasks of MRI (considering combinations of (N, K) as $(1, 4000)$, $(2, 2000)$, and $(4, 1000)$), SP, and NDB (considering combinations of (N, K) as $(4, 5000)$, $(10, 2000)$, and $(20, 1000)$).

The results show that the combination we selected (for each task), on average, returns the best results.

H. Limitations and future work

In this paper, we assume full access to the forward model and focus on 2D image recovery problems. In future work, we aim to extend UGoDIT to 3D image reconstruction and to the blind setting, where the goal is to jointly reconstruct the image and estimate the forward operator.

Additionally, our out-of-distribution (OOD) performance varies across tasks, as discussed in Appendix A. Specifically, for MRI, our OOD performance is lower than that of independently running aSeqDIP. In contrast, for super-resolution (SR), we observe improved acceleration while slightly outperforming aSeqDIP in terms of PSNR. As such, for future work, we will explore combining our method with test-time adaptation approaches to enhance performance on OOD test cases.

I. Implementation details for baselines

Natural image restoration baselines: For Diffusion-based approaches, we use the authors’ official code for each method: DPS with the DDPM solver using 1,000 diffusion steps; SITCOM with $N = 20$ diffusion steps where $K = 20$ optimization steps are used for each. These methods use the pre-trained DM (trained on FFHQ) from DPS. For STRAINER, the Shared INR architecture consists of a single shared encoder—composed of six sine-activated layers—and k decoder heads, where k is the number of images to be learned. During training, we jointly train the encoder and all decoders by minimizing the sum of per-decoder mean squared error (MSE) losses using ADAM [44] with a learning rate of 0.001. At test time, we instantiate a new single-decoder INR initialized with the pre-trained encoder weights and train only both using a data-consistency loss tailored to the relevant forward operator.

MRI reconstruction baselines: For DM-based methods, the pre-trained model is from DDS [12]. In DDS, we set $N = 100$ diffusion steps, whereas SITCOM-MRI uses $N = 50$ diffusion steps, $K = 10$ optimization steps, and $\lambda = 0$ (no regularization). For the supervised mode baseline, we adopt the default VarNet configuration, comprising 12 cascades of unrolled reconstruction steps. Optimization is performed with Adam (learning rate 3×10^{-4}) on the FastMRI knee dataset [20], which contains 973 volumes. From each volume, we discard the first and last five slices, then randomly sample 8,000 images from the remaining slices to form the training set.

J. Visualizations

Figure 15 shows the clean versions of 6 training images (top row) and the 20 testing images sampled from the FFHQ dataset that we used in UGoDIT. Figures 16 and 17 present additional MRI visualizations. Samples from the natural image restoration tasks are given in Figure 18 and Figure 19 super resolution and non-linear deblurring, respectively.



Figure 15: Top: the 6 training images. Bottom: the 20 test images.

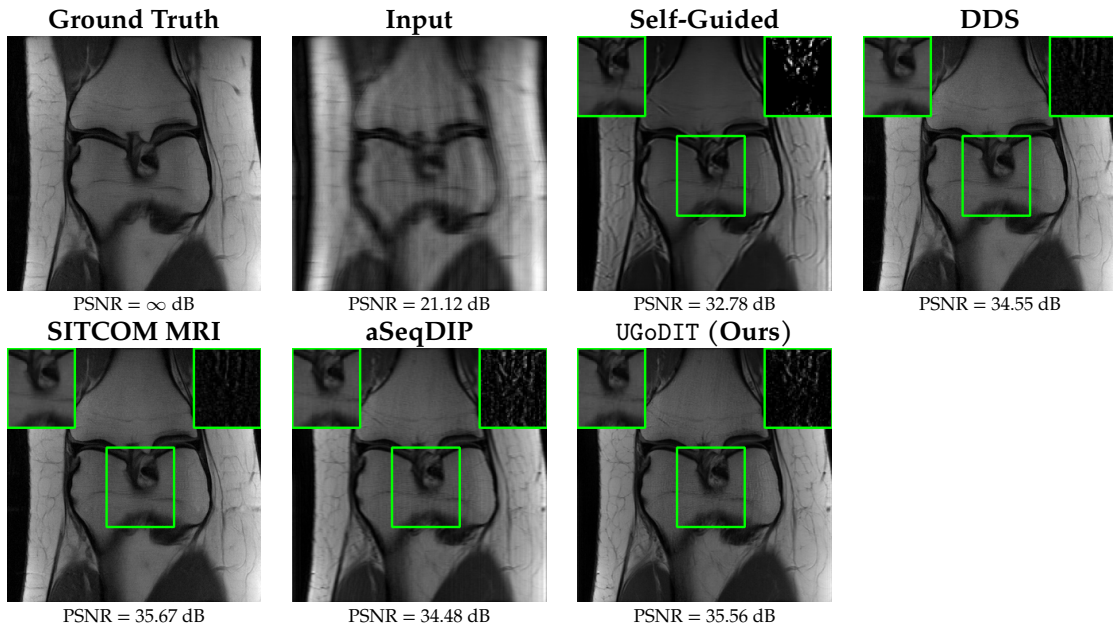


Figure 16: Visualization of ground-truth and reconstructed images using different methods of a knee image from the fastMRI dataset with 4x k-space undersampling. A region of interest is shown with a green box and its error (magnitude) is shown in the panel on the top right.

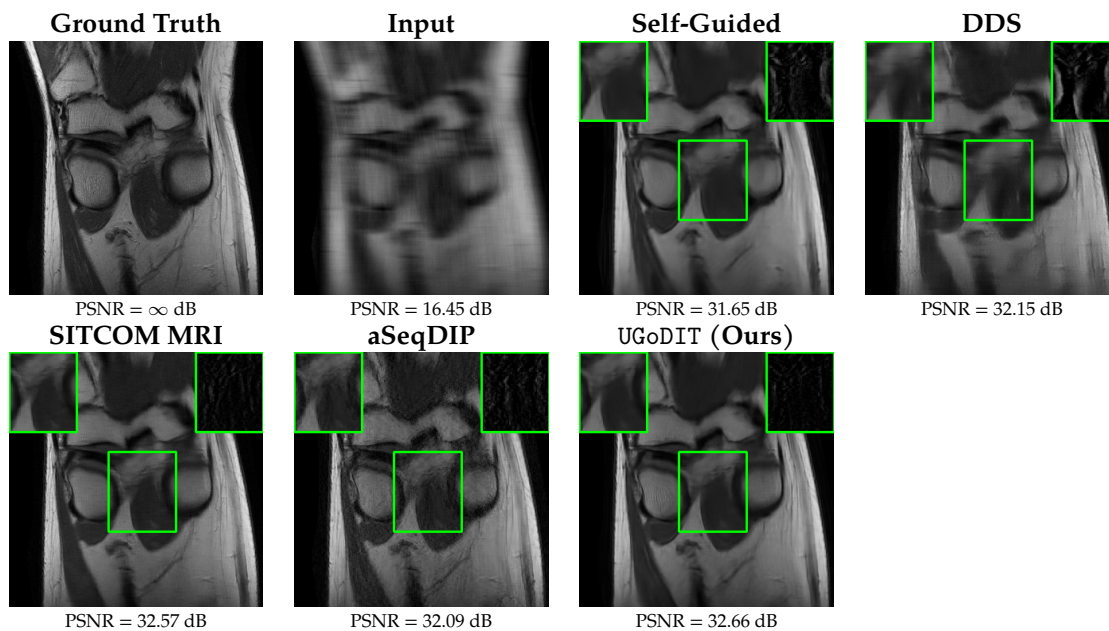


Figure 17: Visualization of ground-truth and reconstructed images using different methods of a knee image from the fastMRI dataset with 8x k-space undersampling. A region of interest is shown with a green box and its error (magnitude) is shown in the panel on the top right.

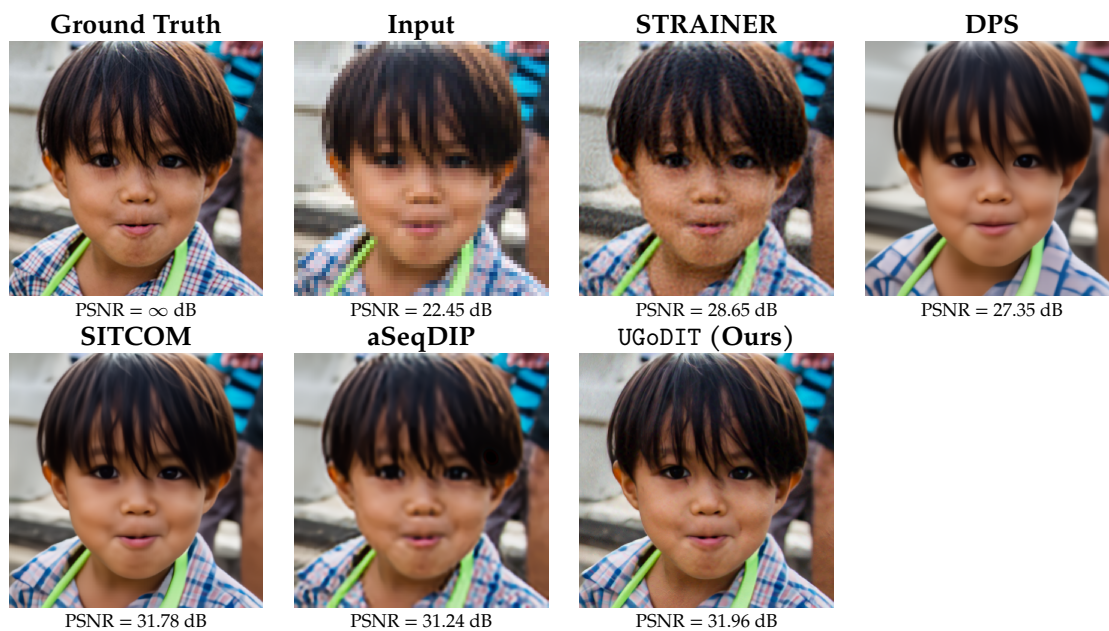


Figure 18: Super Resolution example from the FFHQ dataset.

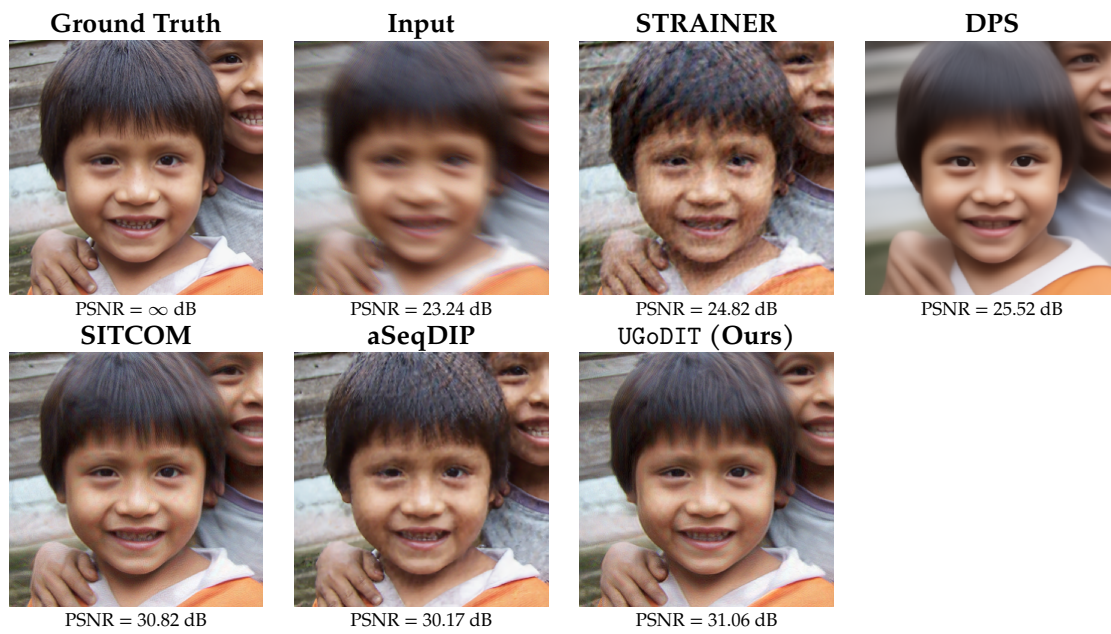


Figure 19: Non-linear deblurring example from the FFHQ dataset.